Atmos. Chem. Phys. Discuss., 15, 3907–3953, 2015
www.atmos-chem-phys-discuss.net/15/3907/2015/
doi:10.5194/acpd-15-3907-2015

Atmospheric Chemistry and Physics
Discussions
Open Access

Vertical profiles of optical and microphysical particle properties above the northern Indian Ocean during CARDEX 2012

F. Höpner[1], F. A.-M. Bender[1], A. M. L. Ekman[1], P. S. Praveen[2], C. Bosch[3], J. A. Ogren[4], A. Andersson[3], Ö. Gustafsson[3], and V. Ramanathan[5]

[1]Department of Meteorology (MISU) and the Bolin Centre for Climate Research, Stockholm University, Stockholm, Sweden
[2]International Centre for Integrated Mountain Development, Kathmandu, Nepal
[3]Department of Environmental Science and Analytical Chemistry (ACES) and the Bolin Centre for Climate Research, Stockholm University, Stockholm, Sweden
[4]Earth System Research Laboratory, National Oceanic and Atmospheric Administration, Boulder Colorado, USA
[5]Scripps Institute of Oceanography, University of California, San Diego, USA

Received: 19 December 2014 – Accepted: 21 January 2015 – Published: 12 February 2015

Correspondence to: F. Höpner (friederike@misu.su.se)

Published by Copernicus Publications on behalf of the European Geosciences Union.

Abstract

A detailed analysis of optical and microphysical properties of aerosol particles during the dry winter monsoon season above the northern Indian Ocean is presented. The Cloud Aerosol Radiative Forcing Experiment (CARDEX), conducted in February and March 2012 at the Maldives Climate Observatory on Hanimaadhoo island (MCOH) in the Republic of the Maldives, used autonomous unmanned aerial vehicles (AUAV) to perform vertical in-situ measurements of particle number concentration, particle number size distribution as well as particle absorption. These measurements were used together with surface-based Mini Micro Pulse Lidar (MiniMPL) observations and aerosol in-situ and off-line measurements to investigate the vertical distribution of aerosol particles.

Air masses were mainly advected over the Indian subcontinent and the Arabian Peninsula. Mean surface aerosol number concentration was $1717 \pm 604\,\mathrm{cm^{-3}}$ and the highest values were found in air masses from the Bay of Bengal and Indo–Gangetic Plain ($2247 \pm 370\,\mathrm{cm^{-3}}$). Investigations of the free tropospheric air showed that elevated aerosol layers with up to 3 times higher aerosol number concentrations than at the surface occurred mainly during periods with air masses originating from the Bay of Bengal and the Indo–Gangetic Plain. Compared to the Indian Ocean Experiment (INDOEX) conducted in winter 1999, elevated aerosol layers with increased aerosol number concentration were observed more frequently in 2012. However, lower particle absorption at the surface ($\sigma_{\mathrm{abs}}(520\,\mathrm{nm}) = 8.5 \pm 4.2\,\mathrm{Wm^{-1}}$) was found during CARDEX compared to INDOEX 1999.

By combining vertical in-situ measured particle absorption with scattering calculated with Mie-theory, layers with single-scattering albedo (SSA) values of specific source regions were derived and utilized to calculate vertical particle absorption profiles from MiniMPL profiles. SSA surface values for dry conditions were found to be 0.94 ± 0.02 and 0.91 ± 0.02 for air masses from the Arabian Sea (and Middle East countries) and India (and Bay of Bengal), respectively. Lidar-derived particle absorption profiles showed

ACPD

15, 3907–3953, 2015

Vertical profiles of optical and microphysical particle properties

F. Höpner et al.

both a similar magnitude and structure as the in-situ profiles measured with the AUAV. However, primarily due to insufficient accuracy in the SSA estimates, the lidar-derived absorption profiles have large uncertainties and are generally weakly correlated to vertically in-situ measured particle absorption.

Furthermore, the mass absorption efficiency (MAE) for the northern Indian Ocean during the dry monsoon season was calculated to determine equivalent black carbon (EBC) concentrations from particle absorption measurements. A mean MAE of 11.6 and 6.9 $m^2 g^{-1}$ for 520 and 880 nm, respectively, was found, likely representing internally mixed BC containing particles. Lower MAE values for 880 nm were found for air masses originating from dust regions such as the Arabian Peninsula and western Asia (5.6 $m^2 g^{-1}$) or from closer source regions as southern India (4.3 $m^2 g^{-1}$).

1 Introduction

Anthropogenic aerosols influence the Earth's energy budget as aerosols can directly scatter and absorb solar radiation and affect cloud radiative properties (Boucher et al., 2013). Whereas the net direct radiative forcing of anthropogenic aerosols is an estimated cooling of −0.35 (±0.5) Wm^{-2}, black carbon (BC) containing particles contribute to a positive direct radiative forcing at the top of the atmosphere (TOA) of +0.4 (+0.05 to +0.8) Wm^{-2} (Boucher et al., 2013).

The term BC is a qualitative description of light-absorbing carbonaceous substances, produced by fossil fuel combustion and biomass burning (Bond et al., 2013; Petzold et al., 2013). Lacking an uniform definition, BC measured by optical methods in the present study is referred to as the equivalent black carbon (EBC) in accordance to Petzold et al. (2013).

Even though BC is estimated to be one of the most important sources for human-caused changes in atmospheric heating next to carbon dioxide, its positive radiative impact is uncertain (Bond et al., 2013). A very recent study by Samset et al. (2014) shows that global aerosol-climate models tends to overestimate the radiative forcing in remote regions and at high altitudes compared to an indicated general underestimation of global BC radiative forcing in atmospheric models (Bond et al., 2013; Andreae and Ramanathan, 2013). Thus, observations are still needed to gain a better understanding of BC physical and chemical properties. In-situ measurements of the vertical profile of BC-containing particles are of particular interest for radiative forcing calculations, but have been performed only occasionally (e.g. Babu et al., 2008, 2011; Corrigan et al., 2008; Wofsy, 2011; Oshima et al., 2012; Sheridan et al., 2012).

The emissions of anthropogenic aerosols, in particular absorbing aerosols, are still increasing in Asian countries such as China and India (Granier et al., 2011; Moorthy et al., 2013). During the dry winter monsoon season every year, polluted air masses from southern Asia are transported towards the northern Indian Ocean. Due to large-scale subsidence over the ocean during that period, the vertical dispersion of pollution is reduced and aerosol particles can be transported over long distances (Lelieveld et al., 2001; Lawrence and Lelieveld, 2010).

Several major field campaigns have been performed to investigate the advection of polluted air masses from southern Asia to the pristine northern Indian Ocean in winter time like e.g. the Indian Ocean Experiment (INDOEX) in 1999, the Maldives Autonomous Unmanned Aerial Vehicle Campaign (MAC) and the Integrated Campaign for Aerosols, Gases and Radiation Budget (ICARB) in 2006, leading to the identification of an elevated aerosol layer above the marine boundary layer (MBL), referred to as an Atmospheric Brown Cloud (ABC) (e.g. Ramanathan et al., 2001; Sheridan et al., 2002; Franke et al., 2003; Corrigan et al., 2008; Moorthy et al., 2008). Previous studies have revealed a significant atmospheric heating and surface cooling by ABCs (e.g. Ramanathan et al., 2001, 2007; Satheesh et al., 2008).

Aerosol measurements at the surface will not necessarily indicate the presence of elevated aerosol layers since the vertical exchange between the MBL and free troposphere (FT) can be weak (e.g. Corrigan et al., 2008). Thus, detailed vertical aerosol profiles are necessary to obtain complete information of the elevated aerosol layer composed of light-scattering and absorbing aerosols.

ACPD
15, 3907–3953, 2015

The present study is based on the field campaign Cloud Aerosol Radiative Forcing Experiment (CARDEX) (see also Bosch et al., 2014; Pistone et al., 2015), which was conducted in the vicinity of the Maldives Climate Observatory in Hanimaadhoo (MCOH) in February and March 2012. CARDEX was conducted by the Scripps Institution of Oceanography at the University of California at San Diego, in collaboration with the Desert Research Institute, Stockholm University, Argonne National Laboratory and the Max Planck Institute in Hamburg. The focus of the study is on the vertical profiles of long-range transported absorbing aerosols over the northern Indian Ocean under cloud-free conditions, utilizing a combination of surface and vertical in-situ measurements as well as ground-based remote sensing instruments.

MCOH, located at 6.78° N, 73.18° E on one of the northernmost Maldives islands (Thiladhummathi Atoll) was founded as a part of the Atmospheric Brown Cloud project in 2004 to investigate the interaction between aerosols, radiation and climate over the Indian Ocean during different monsoon periods (Ramana and Ramanathan, 2006). During the winter monsoon and pre-monsoon, MCOH is a receptor site of long-range transported pollutants from emission regions of South Asia, the Middle East and Africa. Local pollution levels are usually low since MCOH is at the northern tip of the island and the wind direction is dominantly north-easterly during the dry monsoon season. Therefore the Maldives islands in general, and MCOH in particular, offer favourable conditions for the study of processed anthropogenic aerosols.

Here, a detailed analysis of air mass origin is performed, relating source regions to microphysical and optical particle properties. Furthermore, typical vertical aerosol profiles occurring during the dry monsoon season are studied. In particular, the dependence of single scattering albedo (SSA) on air mass source region is investigated. Vertical in-situ measurements, performed with three autonomous unmanned aerial vehicles (AUAV) during CARDEX, are compared with ground-based lidar measurements of aerosol extinction. Furthermore, an approach for estimating particle absorption from lidar measurements and characteristic SSA profiles is presented, and evaluated against vertical in-situ measurements (see Fig. 1). Hereby we investigate the possibility of us-

ACPD
15, 3907–3953, 2015

ing ground-based lidar measurements to determine and monitor the vertical distribution of absorbing aerosols in the area, and evaluate the main sources of uncertainty related to such an approach.

Air mass source- and site-specific Mass Absorption Efficiencies (MAE) are calculated from surface absorption EC mass concentration measurements. This MAE is then used to estimate an EBC concentration from absorption measurements only.

2 Experimental methods

2.1 Autonomous unmanned aerial vehicles

During CARDEX, three AUAVs were used to obtain vertical profiles up to 3 km of aerosol properties, cloud microphysics, turbulence and water vapour fluxes as well as radiation. Robotic aircraft were used already in the early 1990s to measure general meteorological parameters (Holland et al., 2001). The advanced instruments onboard the AUAV, used during CARDEX, were modified and developed at the Scripps Institution of Oceanography (Corrigan et al., 2008).

18 CARDEX research flights were performed from an airport, located around 3 km southwest of MCOH, between 23 February and 26 March 2012. The payload on the aerosol AUAV was a TSI condensation particle counter (Model 3007) that measured the total particle number concentration for aerosol particles with diameter larger than $D_p = 10$ nm. The instrument accuracy of the AUAV CPC was within ±10 %. Furthermore, an optical particle counter (OPC, MetOne Model 9722) that determines the particle number size distribution in 8 channels between $D_p = 0.3$ µm and $D_p = 3.5$ µm was installed. The OPC was calibrated with PSL particles with a refractive index of $m = 1.59 + 0.0i$. A modified Magee AE-31 aethalometer that detects the attenuation of light of a particle-loaded filter for three wavelengths (370, 520, 880 nm) was also deployed. From the light attenuation, particle absorption can be calculated (see Sect. 2.3). The uncertainty of the AUAV aethalometer can range from 5 to 40 % (Corrigan et al.,

ACPD
15, 3907–3953, 2015

2006). General meteorological parameters such as relative humidity, pressure and temperature were also measured with a vertical resolution of 1–4 m.

The maximum flight time of the AUAV was 5 h (Corrigan et al., 2008). For detecting the particle absorption with the Aethalometer, the AUAV needed to stay at a constant altitude for about 20 min (level flight) because variations in pressure, temperature and relative humidity give an unstable signal (Corrigan et al., 2008). Thus, for each single flight, several level flights were performed, usually on the descending flight, to measure the particle absorption. Typically, a flight with the aerosol instrument took around 1.5 h. A full description of the aerosol AUAV and its payload can be found in Corrigan et al. (2008).

2.2 Mini Micro Pulse Lidar

In addition to the in-situ measurements on the AUAV, a Mini Micro Pulse Lidar system (MiniMPL) from SigmaSpace was used to measure the 180° particle backscatter at 532 nm. From these measurements, the vertical particle extinction can be determined with an assumed lidar ratio. The MiniMPL is based on standard MPL systems, first described by Spinhirne (1993) and Spinhirne et al. (1995). It has a single channel at 532 nm with a pulse repetition frequency (PRF) of 4000 Hz. Transmitted laser pulses are scattered back from molecules, aerosols and clouds in the atmosphere. The backscattered signal is received by photodiode detectors and converted into a height profile by measuring the time between transmittance and detection of the laser pulse (Welton et al., 2002).

With the high PRF, a good signal-to-noise ratio can be achieved due to averaging many low-energy pulses in a short time (Spinhirne, 1993). The MiniMPL can detect the near-range atmosphere from about 250 m up to 15 km with a vertical resolution of 30 m. The low minimum range and high spatial resolution make the MiniMPL suitable for comparison with the in-situ AUAV measurements.

The raw signal was corrected for different instrumental and background effects. In the near range of the telescope the signal can usually not be accurately imaged because

ACPD
15, 3907–3953, 2015

of the difference in the transmitter and receiver field of view (overlap error) (Welton et al., 2002). Even though the overlap is considered to be 100 % for the MiniMPL, a geometrical factor calibration, referred to as overlap here as well, has to be applied (SigmaSpace, personal communication, 2014). Furthermore, the photodiode detector can release photoelectrons during turn on already before triggering the laser pulse (Welton et al., 2000). This is called the afterpulse noise and needs to be corrected for. The so called background noise is caused by the sunlight. The measured signal in between two pulses is referred to as the background signal and must be subtracted from the final signal (Welton et al., 2000).

2.3 Stationary instruments at the Maldives Climate Observatory Hanimaadhoo (MCOH)

Continuous measurements of physical and chemical particle properties, solar radiation and meteorological parameters have been performed regularly at MCOH since 2004. The instruments for measuring the solar radiation and meteorological parameters (temperature, relative humidity, pressure, wind, precipitation) were mounted on top of a 15 m tower, which is higher than the surrounding canopy. Hence, the local vegetation should not affect the measurements. The aerosol instruments were located inside the station and sampling of aerosols was done through a 15 m long inlet close to the tower. An impactor at the top of the inlet pipe ensured that particles with a diameter $D_p > 10\,\mu m$ were removed, resulting in collection of PM_{10} (particles with $D_p \leq 10\,\mu m$). The collection efficiency was better than 90 % for particles with $D_p = 10\,\mu m$ and as high as 98 % for particles with $D_p < 5\,\mu m$ (Corrigan et al., 2006).

MCOH data presented in this study are from several aerosol instruments. A condensation particle counter (TSI CPC, model 3022) measured the total aerosol particle number concentration between the particle diameters $D_p = 10$ nm and $D_p = 10\,\mu m$. Particle scattering coefficient (σ_{scat}) at three different wavelengths (450, 550, 700 nm) was measured with a nephelometer (TSI, model 3563). The sampling air was not dried before the instruments inlet. However, relative humidities ~ 10 % below the ambient relative humidity were detected inside the nephelometer. The nephelometer data were corrected for truncation errors and instrument geometry characteristics (Anderson and Ogren, 1998).

With a 7-wavelength aethalometer (Magee scientific, model AE-31), the particle absorption at 370, 430, 470, 520, 590, 700 and 880 nm was determined. The absorption coefficient (σ_{abs}) was calculated from the aethalometer attenuation according to the method of Arnott et al. (2005) considering the scattering and filter loading effects. Values from Table 1 in Arnott et al. (2005) have been used.

For about half of the field campaign, aerosol number size distributions between D_p = 0.5 µm and D_p = 10 µm were measured by an aerodynamic particle sizer (TSI APS, model 3321). More information on the general instrumentation setup at MCOH can be found in Corrigan et al. (2006) and Ramana and Ramanathan (2006).

Furthermore, fine-particulate matter with particle diameters D_p < 2.5 µm ($PM_{2.5}$) was sampled on pre-combusted quartz-filters for subsequent chemical analysis. Elemental carbon (EC) and organic carbon (OC) mass were determined with the NIOSH 5040 method by a thermal-optical transmission analyzer (Sunset Laboratory) after the field campaign (Bosch et al., 2014).

AERONET (AErosol RObotic NETwork) sun photometer measurements are performed continuously at MCOH and the ground based passive remote sensing instrument measures columnar aerosol optical depth (AOD) under clear sky conditions (Holben et al., 1998). Additionally, e.g. aerosol absorption optical depth (AAOD) and SSA values can be determined. AERONET data used in this study are quality-assured level 2.0 data. All described instruments are summarized in Table 1.

2.4 Trajectory analysis

7-day-backward trajectories were used to determine the origin of the air masses arriving at MCOH in the MBL and FT. The trajectories were calculated with the HYSPLIT model developed by NOAA Air Resource Laboratory (Draxler, 1999). Backward trajectories arriving at heights of 400 and 2000 m were assumed to give a good indication

ACPD
15, 3907–3953, 2015

for the air mass origin within the MBL and FT, respectively. The data were sorted into three different air mass groups for subsequent analysis (see Sect. 3).

2.5 Single scattering albedo profiles

The single scattering albedo (SSA), defined as the ratio of σ_{scat} to the particle extinction coefficient σ_{ext}

$$\text{SSA} = \frac{\sigma_{\text{scat}}}{\sigma_{\text{ext}}}, \tag{1}$$

is an important particle property for describing the absorption ability of aerosols. σ_{ext} is the sum of σ_{scat} and σ_{abs}. The SSA is also needed for deriving absorption from lidar measurements (see Sect. 2.6).

The SSA at the surface was determined from in-situ absorption and scattering measurements at MCOH for this study. SSA is mainly influenced by the aerosol composition and size distribution, which are dependent on the air mass sources. Another important factor is the relative humidity since the particle scattering is enhanced by hygroscopic growth (e.g. Fitzgerald et al., 1982; Clarke et al., 2002; Zieger et al., 2013; Titos et al., 2014). As the air mass origin and relative humidity changes with height, the SSA may therefore also vary in the vertical column.

To determine the varying SSA in the column, vertically resolved particle absorption and scattering measurements are required. During the CARDEX research flights, vertical profiles of particle absorption were measured with an onboard Aethalometer. However, only a couple of measurements could be performed for each flight, as described in Sect. 2.1. Vertical profiles of particle scattering were not measured, but can be calculated with Mie-Theory from combined OPC and CPC vertical measurements. In this study a complex refractive index of $m = 1.59 + 0.0i$ was used to account for the OPC calibration (see Sect. 2.1). Mie-Scattering was calculated at ambient relative humidity since the OPC measurements show ambient particle number size distribution in which particles may have changed in size by hygroscopic growth. Finally, scattering

ACPD
15, 3907–3953, 2015

profiles were calculated for dry atmospheric conditions with the hygroscopic enhancement factor found by Clarke et al. (2002) for the northern Indian Ocean in February and March.

$$f(\mathrm{RH}) = \frac{\sigma_{\mathrm{scat}}(\mathrm{RH})}{\sigma_{\mathrm{scat}}(\mathrm{dry})} = 0.841 \cdot \left(\frac{1 - \mathrm{RH}}{100}\right)^{-0.368} \tag{2}$$

An SSA profile with 4 layers was utilized to account for variations in relative humidity and aerosol composition throughout the vertical column. SSA values in the MBL were based on surface measurements, while SSA in the three FT layers (700–1500, 1500–2500 and 2500–3000 m) were calculated from Mie-scattering and individual in-situ absorption values. Mie-scattering was scaled to the layer mean ambient relative humidity using Eq. (2). Mean SSA values in each layer were then established for different source regions (see Sect. 3.2).

SSA calculations from continuous AERONET sun photometer measurements were not used because of temporal differences compared to the flight times. Only a small number of days with simultaneous AERONET SSA and flight data were available. Furthermore, an altitude dependent SSA is important for the following analysis and can not be provided from AERONET measurements.

2.6 Lidar-derived absorption

With the aid of SSA profiles (see Sect. 2.5) we estimated an absorption coefficient and subsequently an EBC profile from MPL measurements. With the following method, lidar measurements have the potential to provide continuous absorption profiles that can be compared to in-situ measurements (see Fig. 1).

First, the extinction profile from the MiniMPL was calculated from the measured 180° backscatter and an assumed lidar ratio, i.e. the ratio between extinction and 180° backscatter. The lidar ratios used here are based on previous studies over the northern Indian Ocean in the same winter monsoon season. For air masses arriving from the polluted northern part of the Indian subcontinent a lidar ratio of 65 was used, while the

Discussion Paper | Discussion Paper | Discussion Paper | Discussion Paper |

ACPD

15, 3907–3953, 2015

Vertical profiles of optical and microphysical particle properties

F. Höpner et al.

lidar ratio for air coming from southern India, the southern Bay of Bengal and Indonesia was set to 50, in accordance with Franke et al. (2003) (see Sect. 3).

An alternative method for determining the lidar extinction is to use the AERONET AOD. The vertical integration of the extinction profile gives the columnar AOD. Thus, the lidar extinction can be constrained by the AERONET AOD (Welton et al., 2000). This means in turn that the lidar ratio is assumed constant through the column which might not be valid for all profiles.

To determine the particle absorption coefficient from the lidar extinction profile, the SSA profiles as described in Sect. 2.5 for the lidar wavelength 532 nm are used.

$$\sigma_{abs} = \sigma_{ext} - \sigma_{scat} = \sigma_{ext} \times (1 - \mathrm{SSA}) \quad (3)$$

With a given mass absorption efficiency an EBC profile can be calculated from the lidar-derived absorption profile (see Sect. 2.8).

Uncertainties in absorption values are dependent on uncertainties in the SSA calculation and grouping by air mass and height level and hence dependent on accuracy of the in-situ absorption and particle number size distribution measurements. Since lidar extinction profiles will be averaged over about 20 min, the temporal variability will play a role as well.

2.7 Evaluation methods

Different methods were used to evaluate the lidar-derived absorption profiles. The most direct method is the comparison of the lidar-derived absorption profile with the measured absorption profiles from the AUAV aethalometer. However, sparse in-situ absorption data (with uncertainties of up to 40 %) makes it challenging to compare the two different absorption profiles quantitatively.

Thus, an additional comparison method was used based on the assumption that absorption can be related to the particle number concentration measured by the onboard CPC. According to Corrigan et al. (2008), a high correlation between the absorption coefficient and total particle concentration in the vertical is justified. MCOH surface mea-

ACPD
15, 3907–3953, 2015

surements from winter 2006 and 2012 give a reasonable linear correlation ($R^2 = 0.67$) between total particle concentration and particle absorption coefficient for 520 nm. To account for various aerosol types we used different linear relations $\sigma_{abs} = a \times N$ (a – correlation factor, N – total particle number concentration) for different air mass source regions, assuming similar compositions and optical properties for each air mass type. From that an absorption profile can be estimated from AUAV CPC measurements.

2.8 Mass Absorption efficiency

Additionally, an EBC mass concentration can be determined from particle absorption measurements using the mass absorption efficiency (MAE).

$$\mathrm{EBC} = \frac{\sigma_{abs}}{\mathrm{MAE}} \tag{4}$$

MAE describes the efficiency of particle mass absorption and is typically given in $m^2\,g^{-1}$. MAE varies for different aerosol compounds and mixtures and its value needs to be assumed or determined as a function of the aerosol type.

A CARDEX-specific MAE was calculated using σ_{abs} for 880 nm and relating it to the EC mass concentration from filter measurements, as particle absorption at 880 nm is considered to be dominated by BC absorption and BC is mainly composed of EC and hence can be quantified with the filter derived EC mass concentration (e.g. Yang et al., 2009).

3 Results and discussion

3.1 Relationship between aerosol particle properties and source region

During CARDEX, polluted air masses from south and southeast Asia were transported to the Maldives by the northeast monsoon. Therefore, long-range transported polluted

ACPD
15, 3907–3953, 2015

aerosols, including BC-containing particles, could be prevalent observed in February. Furthermore, aerosols, originating from western Asia as well as the Arabian Peninsula, likely including dust particles, were detected. Those air masses which crossed the Arabian Sea were observed mainly in March, towards the beginning of the pre-monsoon season when the surface wind typically changes to a northwesterly direction. Figure 2 shows the 7 day backward trajectories arriving at MCOH at 00:00 and 12:00 UTC in February and March in the MBL and FT. Lidar profiles showed that the MBL height was typically between 400 and 800 m during CARDEX. Microwave radiometer measurements in combination with profiles of the meteorological parameters have shown that the cumulus cloud base typically coincides with the MBL top, indicated by a temperature inversion (Pistone et al., 2015). Visual observations confirmed frequent occurrences of haze layers and shallow convective clouds during CARDEX.

Three main air mass clusters were observed in the MBL: 1. Indo–Gangetic Plain (Pakistan and northern India) + Bay of Bengal (IGP), 2. Southern Asia + Bay of Bengal (+ Indonesia) (SI), 3. Arabian Sea and Arabian Peninsula, Iran, Pakistan or Indian west coast (AS). Those air mass clusters are in accordance to other studies at MCOH (e.g. Gustafsson et al., 2009; Engström and Leck, 2011; Bosch et al., 2014). Even though the Maldives are surrounded by ocean, only two days in the beginning of the campaign were dominated by pristine marine air masses from a southern direction in the MBL. During that time vertical profile measurements were not performed. Thus a marine air mass cluster is not included in the following analysis. In the FT, only the clusters IGP and SI were found. Each prevailing wind direction in the MBL and FT lasted for several days. Air masses were usually arriving from different clusters in the MBL and FT during CARDEX.

3.1.1 Surface particle concentration

The timeseries of PM_{10} total particle number concentration at MCOH and from the 18 research flights shown in Fig. 3 give an overview of the timing of the different air mass periods in the MBL and in the FT. The MBL AUAV and MCOH surface measurements

ACPD
15, 3907–3953, 2015

of particle number concentration are in good agreement (within 12.5 % on average). The mean PM_{10} particle number concentration at MCOH and on the AUAV in the MBL were 1717 ± 604 cm^{-3} and 1650 ± 570 cm^{-3}, respectively. Hourly mean aerosol number concentrations at MCOH ranged from 340 to 3500 cm^{-3}. The lowest values were found during the short period with complete marine air mass origin (10–11 February). Marine air masses are expected to have particle number concentrations between 200 and 800 cm^{-3} (Heintzenberg et al., 2000). This indicates that cases with particle number concentrations above 1000 cm^{-3} are likely to have been influenced by transported continental air masses or local emissions. However, local emissions were found to be low since the OC/EC ratio did not show any clear diurnal cycle which suggests no significant influence from local photochemical processes (Bosch et al., 2014).

Air masses transported with the northeasterly winds from the Indian subcontinent and the Bay of Bengal (cluster IGP) had the highest aerosol number concentrations with an average of 2247 ± 370 cm^{-3}. Those air masses are likely to have passed over the highly polluted Indo–Gangetic Plain in northern India and Pakistan. The mean aerosol number concentrations for the Arabian sea (cluster AS) and southern India (cluster SI) aerosols were 1375 ± 531 and 1660 ± 523 cm^{-3}, respectively. Aerosols from SI passed only over the southern tip of India where the particle number concentration and emissions are typically lower than e.g. in northern India (Dey and Di Girolamo, 2010). However, some of those air masses may have passed urban areas in southern India like Bangalore, Chennai or Trivandrum which are known for high aerosol concentration (Moorthy et al., 2005). Air masses from AS are likely influenced by dust from desert regions in South Asia or the Arabian Peninsula and may be affected by the urban Indian west coast. The lower mean particle number concentration for SI and AS are supported by long-term satellite observations, which show significantly lower AOD values (558 nm) over the Arabian Sea and southern India compared to IGP and the northern Bay of Bengal for the winter and pre-monsoon season (Moorthy et al., 2008; Dey and Di Girolamo, 2010).

Discussion Paper | Discussion Paper | Discussion Paper | Discussion Paper |

ACPD
15, 3907–3953, 2015

Vertical profiles of optical and microphysical particle properties

F. Höpner et al.

3.1.2 AOD

There was a general decrease in the aerosol particle number concentration at the surface from February to March. However, no decrease in AERONET AOD at 500 nm was found. The surface particle number concentration variations do not correlate with the AOD variation ($R^2 = 0.04$) (see Fig. 3a and c). The columnar AOD varies between 0.2 and 0.9 with a mean AOD(500 nm) = 0.42 ± 0.15.

Figure 4 shows the mean AOD field over the northern Indian Ocean and Indian subcontinent derived from the satellite based MODIS instrument (Moderate Resolution Imaging Spectroradiometer) on Terra (e.g. King et al., 2003) for three consecutive two-week periods from 15 February until 31 March 2012 (MODIS collection 5.1 data). High AOD values above the Indo–Gangetic Plain and the outflow region above the Bay of Bengal close to the Indian East coast can be seen in all three time periods. Increasing AOD above the Arabian Sea and southern Asia towards the end of the campaign is consistent with the seasonal development seen in long-term satellite observations shown in Dey and Di Girolamo (2010). March marks the beginning of the pre-monsoon season and northwesterly to westerly winds at the surface transport mainly dust to the Arabian Sea and northern as well as central India. The relatively high mean AOD during the last third of the field campaign, seen in Fig. 3a (AOD(500 nm) > 0.6) and 4c, must be caused by high aerosol concentrations above the mixed layer and/or large dust particles in the MBL since only relatively low particle number concentration were found in the MBL (see Fig. 3c). Relatively high particle number concentrations in the FT during the last 6 flights (see Fig. 3b) indicate that an increase in the FT aerosol burden may have contributed to the high AOD values.

3.1.3 Vertical particle number concentration profiles

Between 1000 and 3000 m altitude, the particle number concentration is quite variable, as indicated by the standard deviation (SD) shown in Fig. 3b. The 18 research flights with the AUAVs could measure PM_{10} particle number concentration in-situ dur-

ACPD
15, 3907–3953, 2015

ing different air mass periods in the MBL and FT. The particle number concentrations in the FT were up to 3 times higher than the concentration in the MBL during elevated pollution plume episodes. Those elevated aerosol layers were mostly unrelated to the surface aerosol concentration. This indicates a boundary layer decoupled from the free troposphere. Only a weak correlation between FT and MBL particle number concentration could be found ($R^2 = 0.31$), in general agreement with Corrigan et al. (2008), who found a correlation coefficient of $R^2 = 0.42$ at MCOH in March 2006.

Figure 5b and c shows the median PM_{10} particle number concentration profiles for the different source regions in the MBL and FT for CARDEX. The particle number concentration is in general rather constant throughout the MBL, as expected for a well-mixed MBL. Periods with aerosols transport from IGP and the Bay of Bengal (4 fligths) generally have a higher particle number concentration in the MBL compared to air originating from southern India (5 flights) and the Arabian Sea (9 flights).

Half of the flights were performed during conditions with FT flow from IGP. Even if the variability is quite large, it is clear that an elevated aerosol layer in the FT appears more often during periods of long-range transport from IGP, whereas air masses arriving from southern India show a decrease of the particle number concentration with height on average.

The median PM_1 number concentration profile is shown in Fig. 5a together with the corresponding profiles from the field campaigns INDOEX in February and March 1999 and MAC in March 2006. Significantly higher particle number concentrations were detected in 2006 and 2012 compared to INDOEX in 1999, in particular above the MBL. The 23 research flights performed during INDOEX showed a mean particle number concentration for particles bigger than $D_p = 6\,\mathrm{nm}$ of $1194 \pm 635\,\mathrm{cm}^{-3}$ in the mixed layer up to 1 km over the Maldives Islands (de Reus et al., 2001) compared to $1215 \pm 350\,\mathrm{cm}^{-3}$ for particles bigger than $D_p = 10\,\mathrm{nm}$ during MAC. The mean particle number concentration during CARDEX was as large as $1520 \pm 740\,\mathrm{cm}^{-1}$ for particles bigger than $D_p = 10\,\mathrm{nm}$. The difference above the MBL is even larger.

ACPD
15, 3907–3953, 2015

A higher columnar aerosol load in 2006 and 2012 could be explained with a general increase in emissions over Asia. Several emission inventories show that the BC, NO_x and SO_2 emissions over India have increased between 1999 and 2010 (Granier et al., 2011). Long-term observations in India showed also that AOD (500 nm) is increasing at a rate of 2.3 % on average compared to 1985 (Moorthy et al., 2013). Another reason for differences in aerosol concentration above the MBL can be different meteorological conditions during the different field campaigns. According to Verver et al. (2001), major wind and relative humidity anomalies were observed in 1999. Especially in February 1999, a stronger northern convergence zone occurred compared to the climatological monthly mean circulation between 1990 and 1999. Verver et al. (2001) identified several convective precipitation events in February 1999 which may have influenced the aerosol particle concentration significantly through wet removal.

The particle number concentration profiles show a completely different structure in 1999, 2006 and 2012. While the INDOEX (1999) vertical profile shows a decrease in particle number concentration with height, the distinct peaks between 1000 and 2500 m detected in the MAC and CARDEX profiles indicate that elevated aerosol layers were associated with larger particle number concentrations or more frequently occuring during the two later campaigns. A small variability for the INDOEX profile indicates similar particle number concentration for all flights. The variability in vertical profiles of particle number concentration during MAC and CARDEX on the other hand is larger. As elevated aerosol layers mainly occur with air masses from IGP and the Bay of Bengal, the difference in particle concentration at higher altitudes could mean that more cases with IGP affected air in the FT were detected during MAC 2006 compared to CARDEX and INDOEX.

Even though elevated aerosol layers were identified by vertical optical measurements during INDOEX (see e.g. Ramanathan et al., 2001; Sheridan et al., 2002; Franke et al., 2003), higher aerosol concentration above the MBL were not detected with in-situ flight measurements of particle number concentration (see Fig. 5a). Possible explanations could be differences in meteorology, timing as well as measurement area between

ACPD
15, 3907–3953, 2015

the different INDOEX measurements and compared to MAC and CARDEX. The flights described by de Reus et al. (2001) during INDOEX cover a large area around the Maldives with measurements as far south as over the southern Indian Ocean (≈ 7° N–7° S and 67–79° E). However, one would expect a greater variation for such a large measurement area which is not the case for the INDOEX flights.

3.1.4 Surface particle optical properties

Table 2 gives an overview of the measured optical properties at MCOH and of the AUAV data compared to previous field campaigns. All properties are given for RH < 40 %, partly calculated with Eq. (2). The particle absorption is related to the air mass source in a similar way as the particle number concentration. For CARDEX, the highest mean particle absorption, 11.2 ± 2.2 $\mathrm{M\,m^{-1}}$, was found for aerosols from IGP and the Bay of Bengal. Significantly lower mean absorption coefficients were measured in air masses from southern India (8.4 ± 4.5 $\mathrm{M\,m^{-1}}$) and the Arabian Sea (5.6 ± 2.8 $\mathrm{M\,m^{-1}}$).

Compared to 1999, the absorption coefficient is smaller in the whole column while the scattering is larger at the surface. The mean absorption coefficient measured at MCOH in February and March 2006 is similar to that measured in 1999, but the mean particle scattering in the MBL is instead comparable to CARDEX. Higher scattering coefficients in 2006 and 2012 are in agreement with the higher particle number concentrations. Lower absorption coefficients in 2012 could possibly be explained by changes in emissions over southern Asia. As a consequence of higher particle scattering and lower absorption the SSA was higher in 2012 and 2006 compared to 1999.

A comparison between ambient surface SSA for 450 nm and AERONET SSA for 439 nm show a weak correlation (R^2 = 0.04) and general higher surface values than the AERONET SSA. However, AERONET SSA data was only available for 16 days for the two month campaign period. Furthermore, AERONET calculates the SSA for the whole column which will be influenced by potential elevated aerosol layers.

ACPD
15, 3907–3953, 2015

3.2 Vertical profiles of particle optical properties

Vertical profiles of particle optical properties were derived from MiniMPL and in-situ aerosol measurements as described in Sect. 2. Table 3 gives the relations used for the AUAV CPC based absorption coefficient as well as the SSA values used for lidar-derived absorption calculations for the different source regions.

Table 3 shows SSA values for 4 different altitude ranges and at air mass specific relative humidity which was determined from mean RH profiles. The relative humidity in the MBL was on average increasing towards the top of the MBL and was set to 80 % for the SSA calculations for all cases since no major differences were found for different source regions. As discussed by Pistone et al. (2015), the FT was observed to be either "wet" or "dry". Low relative humidities were mainly detected during periods with air masses from IGP. This is consistent with the typical large scale subsidence over the northern Indian Ocean (Pistone et al., 2015). The mean SSA for IGP air masses above 1500 m was calculated to be 0.82 for "dry" atmospheric conditions (RH < 40 %). In the lowest FT (700–1500 m), SSA was calculated for RH = 75 % to 0.88 ± 0.026. "Wet" conditions occurred when air masses arrived from southern India and Indonesia (Pistone et al., 2015). The relative humidity for SSA calculation was set to RH = 65 % through the whole FT. SSA in the upper part of the measurement range (2500–3000 m) was calculated to be 0.94 ± 0.04 while the SSA between 700 and 1500 m was similar to the SSA for IGP influenced aerosols but with larger variation (0.89 ± 0.11).

SSA values in an altitude range from 1 to 3 km during INDOEX were found to be 0.85 ± 0.06 for ambient atmospheric conditions (Sheridan et al., 2002), comparable to the present results. The fairly high SD for some of the determined SSA values will lead to an increase in uncertainty of the lidar-derived absorption. The uncertainty of the lidar-derived absorption was calculated to be as high as 50 % in some cases (error propagation) and therefore set to 50 %.

Since the FT was never influenced by air masses from the Arabian Sea during CARDEX, typical examples for FT air from IGP and southern India are shown in the fol-

ACPD
15, 3907–3953, 2015

lowing in combination with the evaluation of the different methods for deriving particle absorption profiles.

3.2.1 Air masses from the Indo–Gangetic Plain in the free troposphere

Figure 6 gives an example of vertical profiles of optical properties for the end of the campaign (24 March 2012) showing the PM_{10} particle number concentration for ascending (upleg) and descending (downleg) flights, the relative humidity, the lidar extinction (with lidar ratio or AOD constrained), scattering calculated using Mie-Theory and absorption measured directly onboard the AUAVs and at MCOH as well as calculated using either the lidar-derived extinction (and SSA values for different altitude regions) or the measured particle number concentration (and the linear relation presented in Table 3) (see Sect. 2). Figure 6 shows also the calculated EBC profile calculated from the specific MAE for CARDEX (see Sect. 3.3).

At the end of the campaign, air masses were coming from AS in the MBL and from IGP in the FT. A distinct elevated aerosol layer with high aerosol concentration between 1500 and 2300 m was detected with the onboard CPC (Fig. 6a). The calculated Mie-scattering less clearly indicates such a peak of particle scattering in the same region. High Mie-scattering in the MBL with lower particle number concentration is likely a result of scattering from larger particles such as dust or sea salt.

The lidar extinction (Fig. 6b) indicates large values in the MBL which is either due to high relative humidity and haze (RH $\approx$ 90 % in MBL), leading to high backscatter signals or due to instrument issues. With the given analytical method for determining absorption, a humidity-caused signal can not be distinguished from an aerosol signal. The increasing extinction measured by the lidar below 1000 m can not be related to aerosols given the nearly constant aerosol number concentration in the MBL. Lidar-derived absorption is therefore only given for the FT.

The lidar extinction derived with a given lidar ratio (Fig. 6b, blue line) shows an increase at around 2000 m which indicates that the lidar measurements capture an elevated aerosol layer. However, the aerosol layer seems to be thinner compared to the one seen by in-situ measurements but the difference in timing of the measurements must also be considered. The lidar profile shown was measured about 8 h later than the flight time to avoid clouds and strong background noise from incoming sun light. Closer investigation of the timeseries of the lidar signal indicates that the elevated aerosol, measured by the flights, weakened significantly during the day. The lidar extinction derived with the lidar ratio most likely captured a newly evolved aerosol layer.

Figure 6b also shows the lidar extinction constrained by co-located AOD measurements (green line). The advantage here is that a lidar profile temporally close to the flight time could be chosen, resulting in a better agreement to the scattering calculated by Mie-Theory.

The two right panels of Fig. 6 show the results from the different methods of absorption profiling and subsequent EBC determination. The lidar-derived absorption is shown with a 50 % uncertainty range. The absorption derived from lidar measurements (with lidar ratio) and mean SSA values seems to capture the actual measured absorption well (red dots). However, it is not consistent with the profile of AUAV CPC derived absorption below 1500 m. High relative humidities towards the top of the MBL may have caused a strong backscattering signal and hence a strong lidar-derived particle absorption. The lidar-derived absorption based on extinction constrained by AERONET AOD and mean SSA overestimates the particle absorption compared to the in-situ measurements (see Fig. 6d). It seems that in general the climatological mean SSA values are too low for this specific day, which might be because of high relative humidities throughout the FT.

A partly plotted particle absorption profile (blue and green dashed lines) show the lidar-derived absorption between 1500 and 2500 m calculated with the actual SSA, which was determined from the Mie-scattering and the in-situ absorption measurements at the altitudes where SSA values are available. Lower lidar-derived absorption (with real SSA) indicates that the SSA actually was larger than the mean value for this altitude range on the flight day. Especially the lidar-derived absorption with real SSA in Fig. 6d represents the in-situ measurements well inside the elevated aerosol layer.

ACPD
15, 3907–3953, 2015

3.2.2 Southern Indian air masses in the free troposphere

Figure 7 shows the corresponding profiles as in Fig. 6 for a day with air masses from southern India in the FT. A significantly lower particle number concentration, Mie-scattering, particle extinction as well as absorption was detected through the whole column on 4 March compared to 24 March 2012. EBC values are calculated to be below 1 $\mu g\,m^{-3}$. However, a weak elevated aerosol layer can be seen between 2000 and 3000 m. Typically, the aerosol number concentration on average decreases constantly with height in air masses from southern India (see Fig. 5) but 4 March shows the highest aerosol number concentration in the free troposphere for this type of air mass (see Fig. 3). The weak elevated aerosol layer can be explained by forest fires in southern India which occurred during that part of the CARDEX campaign, as discussed by Chakrabarty et al. (2014).

The lidar extinction and lidar-derived absorption also indicate the presence of this aerosol layer. The lidar profile with a given lidar ratio in this case was taken around 6 h after the flight measurements, which explains the vertical shift of the aerosol layer. A strong increase in lidar extinction for both methods in the MBL is related to increasing relative humidity towards the MBL. The relative humidity is below 40 % in the FT, while it is up to 90 % in the MBL.

The rightmost panel shows the lidar-derived absorption which was calculated from the lidar extinction constrained by the AERONET AOD instead of using a given lidar ratio. Since this profile is determined at the same time as the flights a better agreement between in-situ measured and lidar-derived absorption is achieved. The relatively high in-situ absorption at around 1500 m can only be achieved with the lidar-derived absorption calculated with the actual SSA. This indicates that the determination of the SSA is the critical factor in the absorption calculation. On the other hand the actual measured absorption may be biased high since no indication for high particle absorption at that altitude can be seen in the particle number concentration profile.

ACPD
15, 3907–3953, 2015

3.2.3 Comparison of absorption values derived with different methods

Figure 8 shows a comparison of the particle absorption derived from the different methods and the in-situ measured absorption. The correlation between the calculated absorption values and the in-situ measured absorption is relatively weak in all cases ($R^2 \leq 0.39$).

The particle absorption calculated from the relation with particle number concentration (see Table 3) shows fairly good agreement with the 1 : 1 line in Fig. 8a. The absorption was calculated for different source regions based on surface measurements. However, air masses from a certain source region might not have the same optical properties in the FT as in the MBL. Further, the correlation shown in Table 3 might be better if several years of observations could have been considered.

Except for some outliers, the absorption calculated with the AOD constrained extinction follows the 1 : 1 line fairly well (Fig. 8c). The correlation coefficient is here the best for the absorption calculated with the actual SSA (open circles). The rather high lidar-derived absorption values above $40\,\mathrm{M\,m^{-1}}$ were found to be from the last two AUAV flight days. The utilized mean SSA values must be much lower than the real SSA during those two days and hence produced high particle absorption.

The absorption values calculated using a given lidar ratio show the poorest correlation with the in-situ observations. One main issue may be the time difference between the flight observations and the lidar profiling. However, the lidar-derived absorption profile follows the general structure of the in-situ measured aerosol profiles in the free troposphere (see Figs. 6 and 7).

A somewhat better agreement was achieved with the use of the actual SSA (see Fig. 8b, open circles). It seems that the correct determination of the SSA is a crucial point in deriving the absorption from lidar measurements. A longer time series of vertical in-situ measurements could help to obtain a better source dependent SSA profile. Direct measurements of vertical scattering profiles as already performed for other air-

ACPD
15, 3907–3953, 2015

craft campaigns (e.g. Sheridan et al., 2012; Johnson et al., 2008) would reduce the uncertainty in absorption calculations.

3.3 CARDEX MAE

Figure 9 shows the comparison between measured EC mass ($PM_{2.5}$) and particle absorption at 880 nm. There is a clear linear relation between the particle absorption at 880 nm and the EC mass (see Sect. 2.8). The highest particle absorption and EC mass was measured during periods with air masses from IGP in the MBL, while the lowest values for both particle properties were detected with AS air mass influences, as discussed in Sect. 3.1.

A specific MAE value for MCOH during the dry monsoon season can be calculated with the method described in Sect. 2.8 (similar to Corrigan et al., 2006). Without any distinction between different source regions, a MAE for EBC at 880 nm is calculated to be 6.9 $m^2 g^{-1}$. Adjusted to 520 nm the EBC MAE would be 11.6 $m^2 g^{-1}$. The adjustment was performed according to Yang et al. (2009) with the assumption that the absorption Ångström exponent is 1 for BC particles.

Bond and Bergstrom (2006) gave a MAE estimate for freshly emitted carbonaceous particles of 7.5 ± 1.2 $m^2 g^{-1}$ for 550 nm. MAE values for internally mixed carbonaceous aerosol is estimated to be around 12.5 $m^2 g^{-1}$ (Bond et al., 2013). The overall EBC MAE for CARDEX of 11.6 $m^2 g^{-1}$ represents processed carbonaceous aerosol particles and is also close to the general estimate by Bond et al. (2013).

Furthermore, specific MAE values for each air mass can be determined using the relation between the σ_{abs}(880 nm) and EC mass (see Table 4). Assuming that the slope of the linear relation determines the MAE, air masses from IGP have an MAE of 6.6 $m^2 g^{-1}$, which is also similar to the overall MAE of 6.9 $m^2 g^{-1}$. Air masses from SI and AS have a significantly lower MAE for 880 nm with 4.3 and 5.6 $m^2 g^{-1}$, respectively. For the Arabian Sea, the lower MAE could be explained by a larger contribution from bigger particles, such as dust, since the MAE decreases with increasing particle size for $D_p \geq 300$ nm (Bond and Bergstrom, 2006). MAE of dust is in general smaller

ACPD
15, 3907–3953, 2015

compared to BC-containing particles as well. Air masses passing over southern India may contain relatively freshly emitted BC particles and these have in general a lower MAE than particles with a longer transport time (Bond et al., 2013). According to Arnott et al. (2005), various multiple scattering correction factors should be used for different internally mixed aerosols. This attempt might additionally change the determination of MAE additionally.

On the other hand, fairly high intercept values for all three source-specific relations indicate that it is not only the slope that determines the MAE. With a larger dataset a more accurate relation could likely be achieved and this will be investigated in future studies. The MAE is used to estimate EBC profiles from the absorption profiles as described in Sect. 2 and shown in Sect. 3.2.

4 Summary and conclusion

This study presented aerosol in-situ and lidar-derived measurements, with a focus on aerosol optical properties, from the field campaign CARDEX that took place during the dry monsoon season, February and March 2012, close to the permanent station MCOH on the northern Maldives island Hanimaadhoo.

Air mass cluster analysis confirmed that elevated aerosol layers occur mainly during air mass influence from the Indian subcontinent. The highest aerosol particle number concentrations through the whole column were found for air masses which passed over the highly polluted Indo–Gangetic Plain and which were then transported over the Bay of Bengal to the northern Indian Ocean.

Comparison with previous field campaigns over the same region (INDOEX in 19999 and MAC in 2006) were presented. Elevated aerosol layers were consistently found in in-situ particle number concentration measurements both during MAC and CARDEX, but not during INDOEX. Particle absorption was lower in CARDEX compared to INDOEX and MAC while the scattering was higher, i.e. the SSA was higher during CARDEX.

Discussion Paper | Discussion Paper | Discussion Paper | Discussion Paper |

ACPD

15, 3907–3953, 2015

Vertical profiles of optical and microphysical particle properties

F. Höpner et al.

A main aim of the study was to investigate the possibility of using ground-based lidar measurements to determine the vertical distribution of absorbing aerosols. In-situ AUAV-based measurements of absorption profiles were thus compared with lidar-derived absorption profiles, where the latter require input of vertically resolved SSA values. SSA values for different altitude intervals and different air masses were estimated using in-situ observations of absorption and particle scattering calculated using Mie-theory. The evaluation of the lidar-derived absorption profiles showed a large sensitivity to the given SSA values. Using campaign-averaged, source-specific, SSA values, the overall shape of the lidar-derived absorption profile appeared reasonable, but the correlation with the in-situ measured absorption values was rather poor ($R^2 = 0.15$). Constraining the lidar-derived extinction to AERONET observed AOD improved the correlation with observations ($R^2 = 0.34$) which is likely due to closer agreement in time with the measurement flights. Longer time series of vertically resolved SSA values may help improve the lidar-derived absorption profiles.

Surface measurements of particle absorption and elemental carbon mass concentration were used to determine a specific mass absorption efficiency (MAE) for the northern Indian Ocean during the dry monsoon season. A mean MAE of 11.6 $m^2\,g^{-1}$ for 520 nm was found. This result represents approximately internally mixed BC containing particles according to Bond et al. (2013) who gave an estimate of 12.5 $m^2\,g^{-1}$ for processed carbonaceous aerosol. Lower MAE values were found for air masses originating from southern India and the Arabian Sea. MAE is necessary for calculating equivalent black carbon concentrations from absorption measurements.

Acknowledgements. The CARDEX field campaign was sponsored and funded by the National Science foundation and conducted by the Scripps Institution of Oceanography at the University of California at San Diego in collaboration with the Desert Research Institute, Stockholm University, Argonne National Laboratory and the Max Planck Institute at Hamburg. V. Ramanathan is the principal investigator of CARDEX, E. Wilcox is the Co-PI and H. Nguyen was the field director who conducted the campaign with full support by the government of Maldives. C. Bosch, A. Andersson and Ö. Gustafsson also acknowledge financial support from the Swedish funding agencies FORMAS (214-2009-970), STEM (35450-2), and Sida (AKT-2010-038). C. Bosch

ACPD
15, 3907–3953, 2015

acknowledges additional financial support from EU Marie Curie Programme (PIEF-GA-2011-198507).

Full details of the CARDEX campaign can be found in: http://www-ramanathan.ucsd.edu/files/CARDEX_prop_Jun_20.pdf. This study is Paper#2 from the CARDEX campaign.

References

Anderson, T. L. and Ogren, J. A.: Determining aerosol radiative properties using the TSI 3568 Integrating Nephelometer, Aerosol Sci. Tech., 29, 57–69, 1998. 3916

Andreae, M. O. and Ramanathan, V.: Climates dark forcings, Science, 340, 280–281, 2013. 3911

Arnott, W. P., Hamasha, K., Moosmüller, H., Sheridan, P. J., and Ogren, J. A.: Towards aerosol light-absorption measurements wwith 7-wavelength Aethalometer: evaluation with a photoacoustic instrument and 3-wavelength Nephelometer, Aerosol Sci. Tech., 39, 17–29, 2005. 3916, 3933

Babu, S., Satheesh, S., Moorthy, K., Dutt, C., Nair, V. S., Alappattu, D. P., and Kunhikrishnan, P.: Aircraft measurements of aerosol black carbon from a coastal location in the north-east part of peninsular India during ICARB, J. Earth Syst. Sci., 117, 263–271, 2008. 3911

Babu, S. S., Sreekanth, V., Moorthy, K. K., Mohan, M., Kirankumar, N., Subrahamanyam, D. B., Gogoi, M. M., Kompalli, S. K., Beegum, N., Chaubey, J. P., Kumar, V. A., and Manchanda, R. K.: Vertical profiles of aerosol black carbon in the atmospheric boundary layer over a tropical coastal station: perturbations during an annular solar eclipse, Atmos. Res., 99, 471–478, 2011. 3911

Bond, T. C. and Bergstrom, R. W.: Light absorption by carbon particle: an investigative review, Aerosol Sci. Tech., 40, 27–67, 2006. 3932

Bond, T. C., Doherty, S. J., Fahey, D. W., Forster, P. M., Berntsen, T., DeAngelo, B. J., Flanner, M. G., Ghan, S., Kärcher, B., Koch, D., Kinne, S., Kondo, Y., Quinn, P. K., Sarofim, M. C., Schultz, M. G., Schulz, M., Venkataraman, C., Zhang, H., Zhang, S., Bellouin, N., Guttikunda, S. K., Hopke, P. K., Jacobson, M. Z., Kaiser, J. W., Klimont, Z., Lohmann, U., Schwarz, J. P., Shindell, D., Storelvmo, T., Warren, S. G., and Zender, C. S.: Bounding the role of black carbon in the climate system: a scientific assessment, J. Geophys. Res.-Atmos., 118, 5380–5552, 2013. 3910, 3911, 3932, 3933, 3934

ACPD
15, 3907–3953, 2015

Bosch, C., Andersson, A., Kirillova, E., Budhavant, K., Tiwari, S., Praveen, P. S., Russel, L. M., Beres, N. D., Ramanathan, V., and Gustafsson, Ö.: Source-diagnostic dual-isotope composition and optical properties water-soluble organic carbon and elemental carbon in South Asian outflow intercepted over the Indian Ocean, J. Geophys. Res., 119, 11743–11759, 2014. 3912, 3916, 3921, 3922

Boucher, O., Randall, D., Artaxo, P., Bretherton, C., Feingold, G., Forster, P., Kerminen, V.-M., Kondo, Y., Liao, H., Lohmann, U., Rasch, P., Satheesh, S. K., Sherwood, S., Stevens, B., and Zhang, X. Y.: Clouds and aerosols, in: Climate Change 2013: The Physical Science Basis. Contribution of Working Group I to the Fifth Assessment Report of the Intergovernmental Panel on Climate Change, Cambridge University Press, Cambridge, UK and New York, NY, USA, 614–623, 2013. 3910

Chakrabarty, R. K., Nicholas, D. B., Moosmüller, H., China, S., Mazzoleni, C., Dubey, M. K., Liu, L., and Mishchenko, I.: Soot superaggregates from flaming wildfires and their direct radiative forcing, Nature, scientific report, 4, 5508, doi:10.1038/srep05508, 2014. 3930

Clarke, A. D., Howell, S. G., Quinn, P. K., Bates, T. S., Ogren, J., Andrews, E. A. J., Massling, A., Mayol-Bracero, O., Maring, H., Savoie, D., and Cass, G. R.: INDOEX aerosl: a comparison and summary of chemical, microphysical, and optical properties observed from land, ship, and aircraft, J. Geophys. Res., 107, D198033, doi:10.1029/2001JD000572, 2002. 3917, 3918

Corrigan, C. E., Ramanathan, V., and Schauer, J. J.: Impact of monsoon transitions on the physical and optical properties of aerosols, J. Geophys. Res., 111, D18208, doi:10.1029/2005JD006370, 2006. 3913, 3915, 3916, 3932

Corrigan, C. E., Roberts, G. C., Ramana, M. V., Kim, D., and Ramanathan, V.: Capturing vertical profiles of aerosols and black carbon over the Indian Ocean using autonomous unmanned aerial vehicles, Atmos. Chem. Phys., 8, 737–747, doi:10.5194/acp-8-737-2008, 2008. 3911, 3913, 3914, 3919, 3924

de Reus, M., Krejci, R., Williams, J., Fischer, H., Scheele, R., and Ström, J.: Vertical and horizontal distributions of the aerosol number concentration and size distribution over the northern Indian Ocean, J. Geophys. Res., 106, 28629–28641, 2001. 3924, 3926

Dey, S. and Di Girolamo, L.: A climatology of aerosol optical and microphysical properties over the Indian subcontinent from 9 years (2000–2008) of Multiangle Imaging Spectroradiometer (MISR) data, J. Geophys. Res., 115, D15204, doi:10.1029/2009JD013395, 2010. 3922, 3923

ACPD

15, 3907–3953, 2015

Vertical profiles of optical and microphysical particle properties

F. Höpner et al.

Draxler, R. R.: HYSPLIT4 User's Guide, Tech. Rep., NOAA Air Resources Laboratory, Silver Spring, MD, 1999. 3916
Engström, J. E. and Leck, C.: Reducing uncertainties associated with filter-based optical measurements of light absorbing carbon particles with chemical information, Atmos. Meas. Tech., 4, 1553–1566, doi:10.5194/amt-4-1553-2011, 2011. 3921
Fitzgerald, J., Hoppel, W., and Vietti, M.: The size and scattering coefficient of urban aerosol pparticle at Washington, DC as a function of relative humidty, J. Atmos. Sci., 39, 1838–1852, 1982. 3917
Franke, K., Ansmann, A., Müller, D., Althausen, D., Venkataraman, C., Reddy, M. S., Wagner, F., and Scheele, R.: Optical properties of the Indo–Asian haze layer over the tropical Indian Ocean, J. Geophys. Res., 108, D24059, doi:10.109/2002JD002473, 2003. 3911, 3919, 3925
Granier, C., Bessagnet, B., Bond, T., D'Angiola, A., Denier van der Gon, H., Frost, G. J., Heil, A., Kaiser, J. W., Kinne, S., Klimont, Z., Kloster, S., Lamarque, J.-F., Liousse, C., Masui, T., Meleux, F., Mieville, A., Ohara, T., Raut, J.-C., Riahi, K., Schultz, M. G., Smith, S. J., Thompson, A., van Aardenne, J., van der Werf, G. R., and van Vuuren, D. P.: Evolution of anthropogenic and biomass burning emissions of air pollutants at global and regional scales during the 1980–2010 period, Climatic Change, 109, 163–190, 2011. 3911, 3925
Gustafsson, Ö., Kruså, M., Zencak, Z., Sheesley, R. J., Granat, L., Engström, E., Praveen, P. S., Rao, P. S. P., Leck, C., and Rodhe, H.: Brown cloud over south Asia: biomass or fossil fuel combustion, Science, 323, 495–498, 2009. 3921
Heintzenberg, J., Covert, D. C., and Van Dingenen, R.: Size distribution and chemical composition of marine aerosols: a compilation and review, Tellus B, 52, 1104–1122, 2000. 3922
Holben, B. N., Eck, T. F., Slutsker, I., Tanre, D., P., B. J., Setzer, A., Vermote, E., Reagan, J. A., Kaufman, Y. J., Nakajima, T., Lavenu, F., Jankowiak, I., and Smirnov, A.: Aeronet – a federated instrument network and data archive for aerosol characterization, Remote Sens. Environ., 66, 1–16, 1998. 3916
Holland, G. H., Webster, P. J., Curry, J. A., Tyrell, G., Gauntlett, D., Brett, G., Becker, J., Hoag, R., and Vaglienti, W.: The aerosonde robotic aircrafts: a new paradigm for environmental observations, B. Am. Meteorol. Soc., 82, 889–901, 2001. 3913
Johnson, B. T., Osborne, S. R., Haywood, J. M., and Harrison, M. A. J.: Aircraft measurements of biomass burning aerosol over West Africa during DABEX, J. Geophys. Res., 113, D00C06, doi:10.1029/2007JD009451, 2008. 3932

ACPD
15, 3907–3953, 2015

King, M. D., Menzel, W. P., Kaufman, Y. J., Tanre, D., Gao, B.-C., Platnick, S., Ackerman, S. A., Remer, L. A., Pincus, R., and Hubanks, P. A.: Cloud and aerosol properties, precipitable water, and profiles of temperature and water vapor from MODIS, IEEE T. Geosci. Remote, 41, 442–458, 2003. 3923

Lawrence, M. G. and Lelieveld, J.: Atmospheric pollutant outflow from southern Asia: a review, Atmos. Chem. Phys., 10, 11017–11096, doi:10.5194/acp-10-11017-2010, 2010. 3911

Lelieveld, J., Crutzen, P. J., Ramanathan, V., Andreae, M. O., Brenninkmeijer, C. A. M., Campos, T., Cass, G. R., Dickerson, R., Fischer, H., de Gouw, J. A., Hansel, A., Jefferson, M. G., Kley, D., de Laat, A. T. J., Lal, S., Lawrence, M. G., Lobert, J. M., mayol Bracero, O. L., Mitra, A. P., Novakov, T., Oltmans, S. J., Prather, K. A., Reiner, T., Rodhe, H., Scheeren, H. A., Sikka, D., and Williams, J.: The Indian Ocean Experiment: widespread air pollution from south and southeast Asia, Science, 291, 1031–1036, 2001. 3911

Moorthy, K. K., Sunilkumar, S. V., Pillai, P. S., Parameswaran, K., Nair, P. R., Ahmed, Y. N., Ramgopal, K., Narasimhulu, K., Reddy, R. R., Vinoj, V., Satheesh, S. K., Niranjan, K., Rao, B. M., Brahmanandam, P. S., Saha, A., Badarinath, K. V. S., Kiranchand, T. R., and Latha, K. M.: Wintertime spatial characteristics of boundary layer aerosols over peninsular India, J. Geophys. Res.-Atmos., 110, D08207, doi:10.1029/2004JD005520, 2005. 3922

Moorthy, K. K., Satheesh, S. K., Babu, S. S., and Dutt, C. B. S.: Integrated Campaign for Aerosols, Gases and Radiation Budget (ICARB): an overview, J. Earth Syst. Sci., 117, 243–262, 2008. 3911, 3922

Moorthy, K. K., Babu, S. S., Manoj, M. R., and Satheesh, S. K.: Buildup of aerosols over the Indian region, Geophys. Res. Lett., 40, 1011–1014, 2013. 3911, 3925

Oshima, N., Kondo, Y., Moteki, N., Takegawa, N., Koike, M., Kita, K., Matsui, H., Kajino, M., Nakamura, H., Jung, J. S., and Kim, Y. J.: Wet removal of black carbon in Asian outflow: Aerosol Radiative Forcing in East Asia (A-FORCE) aircraft campaign, J. Geophys. Res.-Atmos., 117, doi:10.1029/2011JD016552, 2012. 3911

Petzold, A., Ogren, J. A., Fiebig, M., Laj, P., Li, S.-M., Baltensperger, U., Holzer-Popp, T., Kinne, S., Pappalardo, G., Sugimoto, N., Wehrli, C., Wiedensohler, A., and Zhang, X.-Y.: Recommendations for reporting "black carbon" measurements, Atmos. Chem. Phys., 13, 8365–8379, doi:10.5194/acp-13-8365-2013, 2013. 3910

Pistone, K., Wilcox, E., Praveen, P. S., Thomas, R. M., Bender, F. A.-M., Feng, Y., and Ramanathan, V.: The role of atmospheric properties in aerosol indirect effects in a trade cumulus regime, in preparation, 2015. 3912, 3921, 3927

ACPD
15, 3907–3953, 2015

Vertical profiles of optical and microphysical particle properties

F. Höpner et al.

Ramana, M. V. and Ramanathan, V.: Abrupt transition from natural to anthropogenic aerosol radiative forcing: observations at the ABC-Maldives Climate Observatory, J. Geophys. Res., 111, D20207, doi:10.1029/2006JD007063, 2006. 3912, 3916

Ramanathan, V., Crutzen, P. J., Lelieveld, J., Mitra, A. P., Althausen, D., Anderson, J., Andreae, M. O., Cantrell, W., Cass, G. R., Chung, C. E., Clarke, A. D., Coakley, J. A., Collins, W. D., Conant, W. C., Dulac, F., Heintzenberg, J., Heymsfield, A. J., Holben, B. N., Howell, S. G., Hudson, J., Jayaraman, A., Kiehl, J. T., Krishnamurti, T. N., Lubin, D., McFarquhar, G., Novakov, T., Ogren, J. A., Podgorny, I. A., Prather, K. A., Priestley, K., Prospero, J. M., Quinn, P. K., Rajeev, K., Rasch, P., Rupert, S., Sadourny, R., Satheesh, S. K., Shaw, G. E., Sheridan, P., and Valero, F. P. J.: Indian Ocean Experiment: an integrated analysis of the climate forcing and effects of the great Indo–Asian haze, J. Geophys. Res., 106, 28371–28398, 2001. 3911, 3925

Ramanathan, V., Ramana, M. V., Roberts, G. C., Kim, D., Corrigan, C. E., Chung, C. E., and Winker, D.: Warming trends in Asia amplified by brown cloud solar absorption, Nature, 448, 575–578, 2007. 3911

Samset, B. H., Myhre, G., Herber, A., Kondo, Y., Li, S.-M., Moteki, N., Koike, M., Oshima, N., Schwarz, J. P., Balkanski, Y., Bauer, S. E., Bellouin, N., Berntsen, T. K., Bian, H., Chin, M., Diehl, T., Easter, R. C., Ghan, S. J., Iversen, T., Kirkevåg, A., Lamarque, J.-F., Lin, G., Liu, X., Penner, J. E., Schulz, M., Seland, Ø., Skeie, R. B., Stier, P., Takemura, T., Tsigaridis, K., and Zhang, K.: Modelled black carbon radiative forcing and atmospheric lifetime in AeroCom Phase II constrained by aircraft observations, Atmos. Chem. Phys., 14, 12465–12477, doi:10.5194/acp-14-12465-2014, 2014. 3910

Satheesh, S. K., Moorthy, K. K., Babu, S. S., Vinoj, V., and Dutt, C. B. S.: Climate implications of large warming by elevated aerosol over India, Geophys. Res. Lett., 35, L19809, doi:10.1029/2008GL034944, 2008. 3911

Sheridan, P. J., Jefferson, A., and Ogren, J. A.: Spatial variability of submicrometer aerosol radiative properties over the Indian Ocean during INDOEX, J. Geophys. Res., 107, INX2 10-1–INX2 10-17, doi:10.1029/2000JD000166, 2002. 3911, 3925

Sheridan, P. J., Andrews, E., Ogren, J. A., Tackett, J. L., and Winker, D. M.: Vertical profiles of aerosol optical properties over central Illinois and comparison with surface and satellite measurements, Atmos. Chem. Phys., 12, 11695–11721, doi:10.5194/acp-12-11695-2012, 2012. 3911, 3932

Spinhirne, J. D.: Micro pulse lidar, IEEE T. Geosci. Remote, 31, 48–55, 1993. 3914

ACPD
15, 3907–3953, 2015

Vertical profiles of optical and microphysical particle properties

F. Höpner et al.

Spinhirne, J. D., Rall, J., and Scott, V. S.: Compact eye-safe lidar systems, The Review of Laser Engineering, 23, 26–32, 1995. 3914

Titos, G., Jefferson, A., Sheridan, P. J., Andrews, E., Lyamani, H., Alados-Arboledas, L., and Ogren, J. A.: Aerosol light-scattering enhancement due to water uptake during the TCAP campaign, Atmos. Chem. Phys., 14, 7031–7043, doi:10.5194/acp-14-7031-2014, 2014. 3917

Verver, G. H. L., Sikka, D., Lobert, J. M., Stossmeister, G., and Zachariasse, M.: Overview of the meteorological conditions and atmospheric transport processes during INDOEX 1999, J. Geophys. Res., 106, 28399–28413, 2001. 3925

Welton, E. J., Voss, K. J., Gordon, H. R., Maring, H., Smirnov, A., Holben, B., Schmid, B., and Livingston, J. M., Russell, P. B., Durkee, P. A., Formenti, P., and Andreae, M. O.: Ground-based lidar measurements of aerosols during ACE-2: instrument description, results, and comparisons with other ground-based and airborne measurements, Tellus B, 52, 636–651, 2000. 3915, 3919

Welton, E. J., Voss, K. J., Quinn, P. K., Flatau, P. J., Markowicz, K., Campbell, J. R., Spinhirne, J. D., Gordon, H. R., and Johnson, J. E.: Measurements of aerosol vertical profiles and optical properties during INDOEX 1999 using micropulse lidars, J. Geophys. Res.-Atmos., 107, INX2-1 – INX2-20 doi:10.1029/2000JD000038, 2002. 3915

Wofsy, S.: HIAPER Pole-to-Pole Observations (HIPPO): fine-grained, global-scale measurements of climatically important atmospheric gases and aerosols, Philos. T. R. Soc. A, 369, 2073–2086, 2011. 3911

Yang, M., Howell, S. G., Zhuang, J., and Huebert, B. J.: Attribution of aerosol light absorption to black carbon, brown carbon, and dust in China – interpretations of atmospheric measurements during EAST-AIRE, Atmos. Chem. Phys., 9, 2035–2050, doi:10.5194/acp-9-2035-2009, 2009. 3920, 3932

Zieger, P., Fierz-Schmidhauser, R., Weingartner, E., and Baltensperger, U.: Effects of relative humidity on aerosol light scattering: results from different European sites, Atmos. Chem. Phys., 13, 10609–10631, doi:10.5194/acp-13-10609-2013, 2013. 3917

ACPD
15, 3907–3953, 2015

Table 1. Instruments used during CARDEX at MCOH and onboard the AUAV.

Instrument	Property	Measurement location
SigmaSpace Mini Pulse Lidar (MPL)	Vertical atmospheric backscatter coefficient at $\lambda = 532\,\text{nm}$	MCOH
TSI Condensation particle counter (CPC)	Total aerosol particle number concentration $D_p = 10\,\text{nm} - 10\,\mu\text{m}$	MCOH AUAV
TSI Nephelometer	Particle scattering coefficient $\lambda = 450,\ 550,\ 700\,\text{nm}$	MCOH
Magee Aethalometer	Particle absorption coefficient $\lambda = 370,\ 430,\ 470,\ 520,\ 590,\ 700,\ 880\,\text{nm}$	MCOH AUAV
Met One Optical particle counter (OPC)	Aerosol particle number size distribution $D_p = 0.3 - 3.5\,\mu\text{m}$	AUAV
AERONET sun photometer	(Absorption) Aerosol optical depth (AOD, AAOD), SSA	MCOH
Thermal-optical transmission analyzer	$PM_{2.5}$ EC, OC concentration	MCOH

ACPD
15, 3907–3953, 2015

Table 2. Mean particle properties during CARDEX at the surface and in some cases above the MBL at dry conditions (RH < 40 %) compared to MAC 2006 and INDOEX 1999. Particle properties for CARDEX are given for the different source regions, Indo–Gangetic Plain (IGP), southern India (SI) and Arabian Sea (AS), for BL and FT.

Parameter Wavelength	CARDEX 2012	MAC 2006	INDOEX 1999 (Sheridan et al., 2002)
absorption	BL IGP 11.2 ± 2.2		
coeff. [$\mathrm{M\,m^{-1}}$]	BL SI 8.4 ± 4.5	BL 13.8 ± 5.4	BL 14 ± 7
550 nm	BL AS 5.6 ± 2.8		
	FT IGP 12.7 ± 6.0		1–3 km 16 ± 10
	FT SI 6.6 ± 5.8		
scattering	BL IGP 112 ± 33		
coeff. [$\mathrm{M\,m^{-1}}$]	BL SI 80 ± 29	BL 88.9 ± 41.2	BL 63 ± 29
550 nm	BL AS 81 ± 40		
extinction	BL IGP 123 ± 34		
coeff. [$\mathrm{M\,m^{-1}}$]	BL SI 88 ± 33	BL 138 ± 37	BL 83 ± 48
550 nm	BL AS 87 ± 42		
SSA	BL IGP 0.91 ± 0.02		
550 nm	BL SI 0.91 ± 0.02	BL 0.90 ± 0.03	BL 0.81 ± 0.04
	BL AS 0.94 ± 0.02		

ACPD
15, 3907–3953, 2015

Table 3. Coefficients used to describe the relationship between particle absorption (σ_{abs}) and particle number concentration N for different source regions. Also shown is the mean SSA for various height levels used to calculate the lidar-derived absorption coefficients.

source region	σ_{abs}(532 nm)	SSA surface (at RH = 80 %)	SSA 700–1500 m	SSA 1500–2500 m	SSA 2500–3000 m
Indo–Gangetic Plain	$5.02 \times 10^{-3} \cdot N$ $R^2 = 0.35$	0.94 ± 0.014	0.88 ± 0.026 (at RH = 75 %)	0.82 ± 0.11 (at RH < 40 %)	0.82 ± 0.14 (at RH < 40 %)
Southern India	$5.33 \times 10^{-3} \cdot N$ $R^2 = 0.48$	0.94 ± 0.016	0.89 ± 0.11 (at RH = 65 %)	0.85 ± 0.11 (at RH = 65 %)	0.94 ± 0.04 (at RH = 65 %)
Arabian Sea	$4.24 \times 10^{-3} \cdot N$ $R^2 = 0.63$	0.96 ± 0.012	x	x	x

Discussion Paper | Discussion Paper | Discussion Paper | Discussion Paper |

ACPD

15, 3907–3953, 2015

Vertical profiles of optical and microphysical particle properties

F. Höpner et al.

Table 4. Relation between particle absorption at 880 nm and the $PM_{2.5}$ EC mass concentration for different source regions.

Source region	$\sigma_{abs}(880\,\text{nm}) = a\ m_{EC} + b$	R^2
All together	$\sigma_{abs}(880\,\text{nm}) = 6.9\ m_{EC} - 0.09$	0.81
Indo–Gangetic Plain	$\sigma_{abs}(880\,\text{nm}) = 6.6\ m_{EC} + 0.67$	0.81
Southern India	$\sigma_{abs}(880\,\text{nm}) = 4.3\ m_{EC} + 0.8$	0.83
Arabian Sea	$\sigma_{abs}(880\,\text{nm}) = 5.6\ m_{EC} + 0.4$	0.79

ACPD
15, 3907–3953, 2015

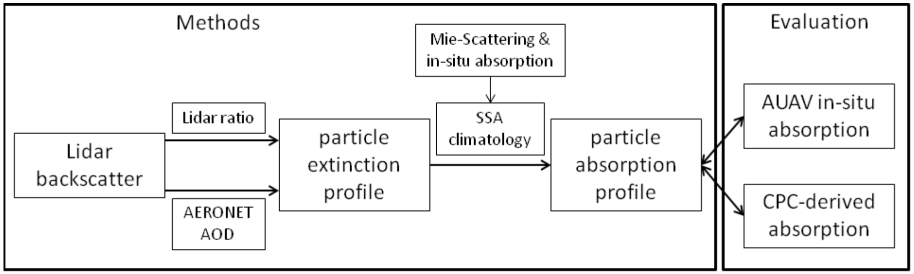

Figure 1. Flow chart describing the derivation of particle absorption profiles from lidar measurements, and their evaluation against in-situ observations.

ACPD
15, 3907–3953, 2015

Vertical profiles of optical and microphysical particle properties

F. Höpner et al.

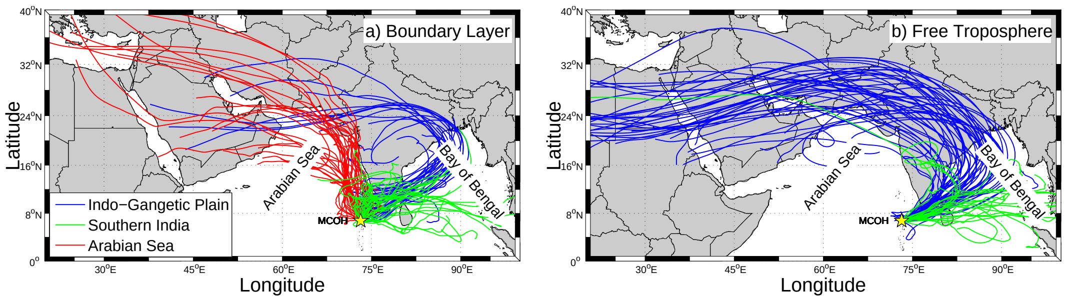

Figure 2. 7-day-backward trajectories calculated by the HYSPLIT model arriving in the MBL at 400 m **(a)** and in the FT 2000 m **(b)** above MCOH at 00:00 and 12:00 UTC each day during CARDEX in February and March 2012. Colours represent the air mass source regions Indo–Gangetic Plain (blue), southern India (green) and the Arabian Sea (red).

ACPD
15, 3907–3953, 2015

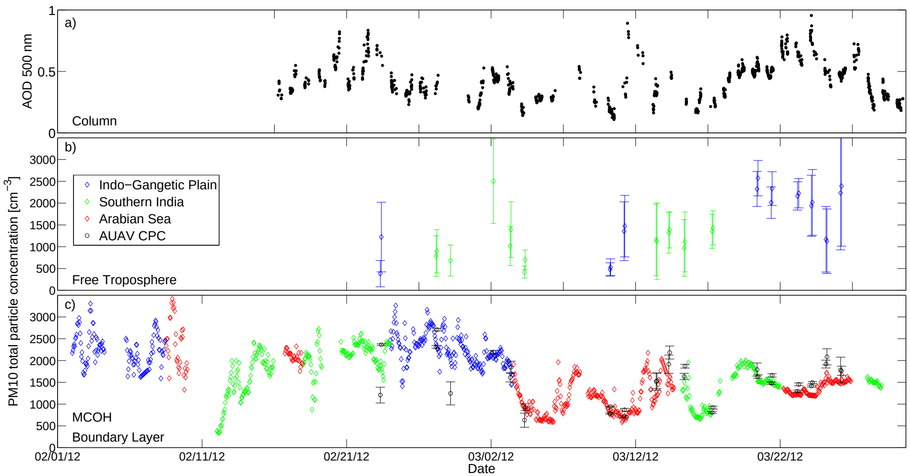

Figure 3. (a) Time series of AOD at 500 nm measured by AERONET sun photometer. **(b)** Time series of the mean total particle concentration with SD in the FT (1000–3000 m) measured by CPC onboard AUAV. **(c)** Time series of PM_{10} total particle concentration measured by CPC at MCOH (colored diamonds) and mean total particle concentration with SD in the MBL (0–500 m) (black circles) measured by the onboard AUAV CPC. The color coding corresponds to the trajectory cluster analysis shown in Fig. 1 (3 clusters in MBL and 2 clusters in FT).

ACPD
15, 3907–3953, 2015

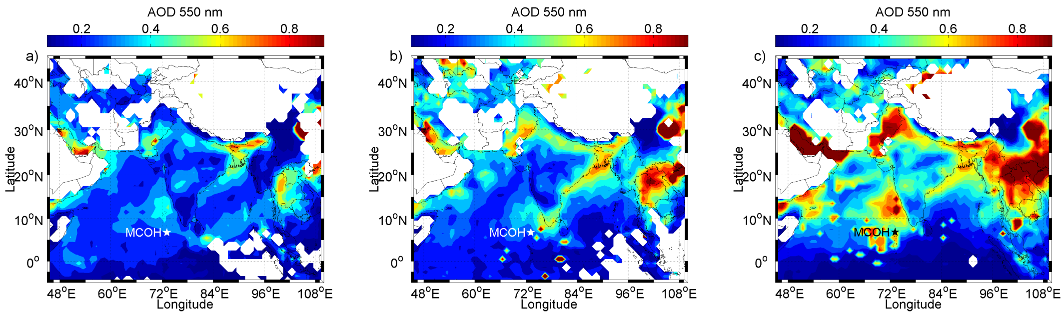

Figure 4. Mean AOD at 550 nm derived from measurements by the MODIS instrument onboard the Terra satellite. **(a)** 15 till 29 February 2012, **(b)** 1 till 15 March 2012. **(c)** 16 till 31 March 2012.

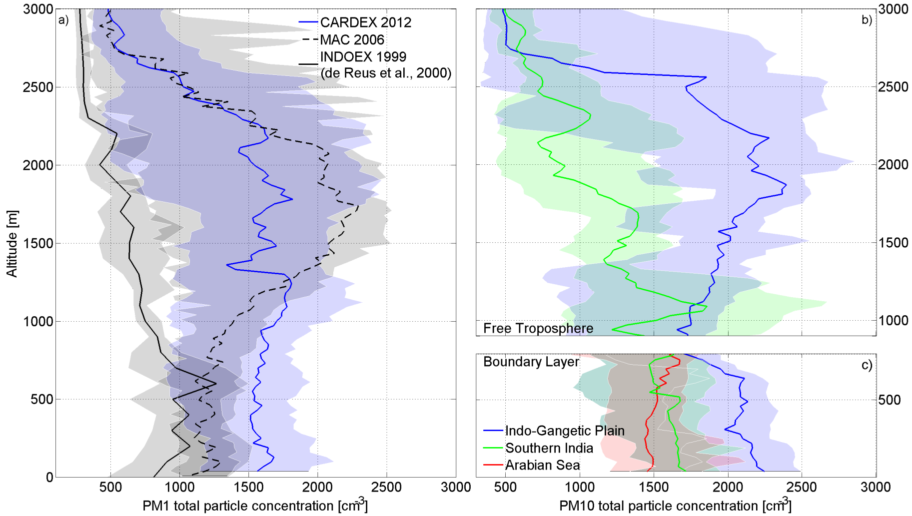

Figure 5. (a) Vertical profile of the median PM_1 particle number concentration during CARDEX (blue), MAC (black dashed) and INDOEX (black solid) with 25 and 75 % percentiles, measured by a CPC onboard the AUAV. **(b)** and **(c)** Median PM_{10} particle number concentration during CARDEX with 25 and 75 % percentiles in the FT and MBL, respectively for air masses originating from the Indo–Gangetic Plain, southern India and Arabian sea (blue, green, red).

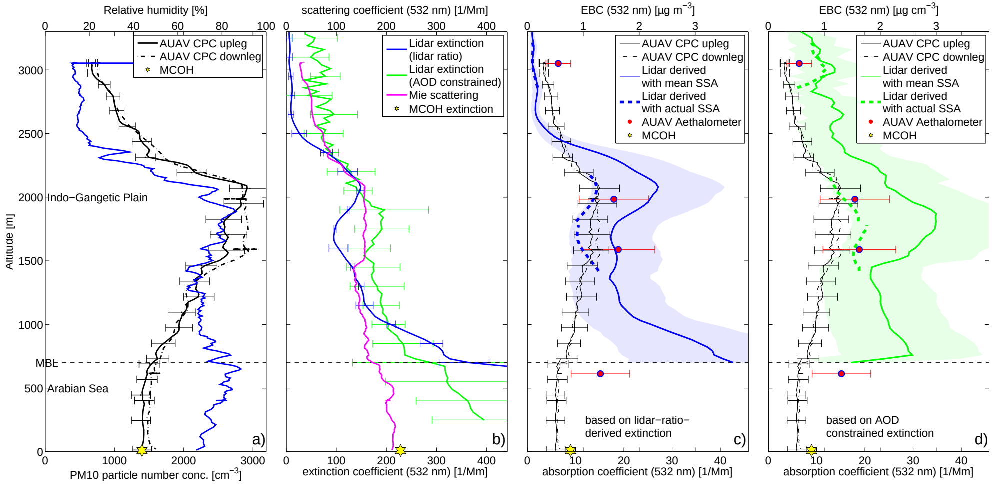

Figure 6. 24 March 2012. **(a)** Profile of PM_{10} particle number concentration measured by AUAV CPC for upleg (black solid) and downleg (black dashed) flights and vertical relative humidity profile (blue). **(b)** Profile of particle extinction measured with the miniMPL (blue), scattering calculated with Mie-Theory (magenta). **(c)** Profile of particle absorption and EBC measured by an onboard aethalometer (red dots), estimated from lidar measurements (blue) with mean SSA and 50 % uncertainty (blue shading), estimated from lidar measurements with actual SSA (blue dashed) and AUAV CPC approach (black). **(d)** Same as **(c)** but with lidar extinction constrained by AERONET AOD (green and green dashed).

ACPD
15, 3907–3953, 2015

Vertical profiles of optical and microphysical particle properties

F. Höpner et al.

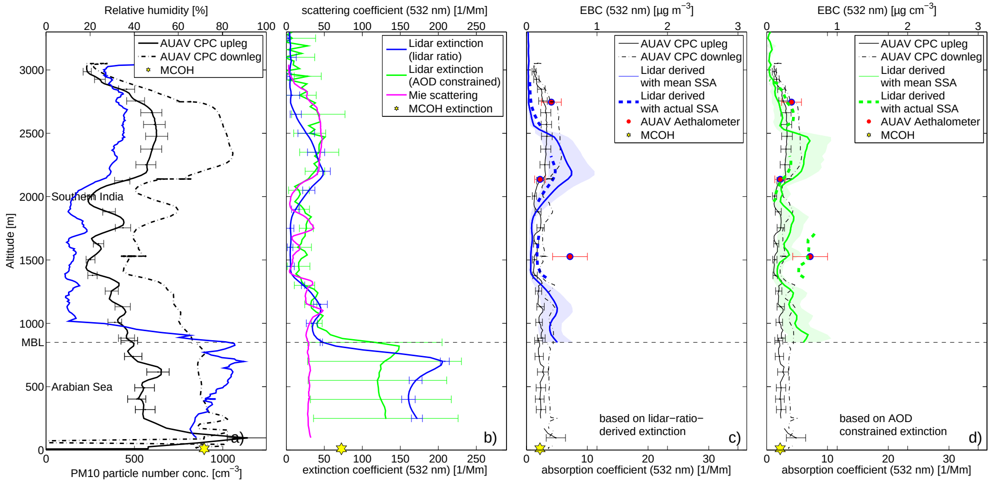

Figure 7. 4 March 2012. **(a)** Profile of PM_{10} particle number concentration measured by AUAV CPC for upleg (black solid) and downleg (black dashed) flights and relative humidity profile (blue). **(b)** Profile of particle extinction measured with the miniMPL (blue), scattering calculated with Mie-Theory (magenta). **(c)** Profile of particle absorption and EBC measured by an onboard aethalometer (red dots), estimated from lidar measurements (blue) with mean SSA and 50 % uncertainty (blue shading), estimated from lidar measurements with actual SSA (blue dashed) and AUAV CPC approach (black). **(d)** Same as **(c)** but with lidar extinction constrained by AERONET AOD (green and green dashed).

ACPD

15, 3907–3953, 2015

Vertical profiles of optical and microphysical particle properties

F. Höpner et al.

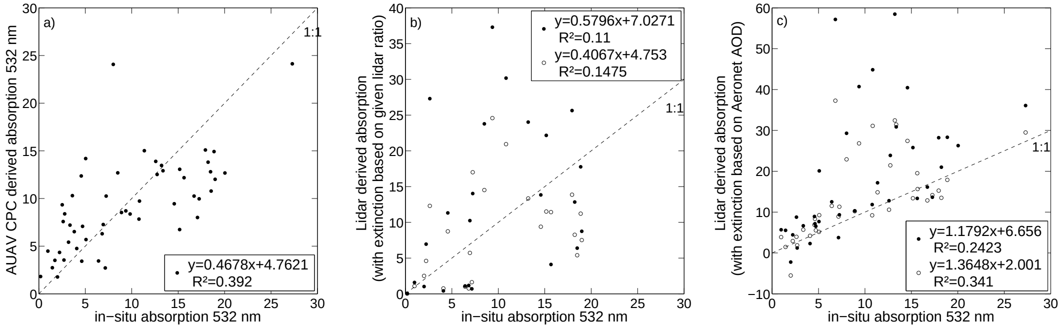

Figure 8. Scatter plot of **(a)** AUAV CPC derived absorption and in-situ absorption, **(b)** Lidar-derived absorption with extinction based on a given lidar ratio depending on air mass source region and source-specific SSA (closed circles) or actual SSA (open circles) against the in-situ absorption and **(c)** Lidar-derived absorption with extinction constrained by the AERONET AOD and source-specific SSA (closed circles) or actual SSA (open circles) against the in-situ absorption. Particle absorption is given for 532 nm.

ACPD
15, 3907–3953, 2015

Vertical profiles of optical and microphysical particle properties

F. Höpner et al.

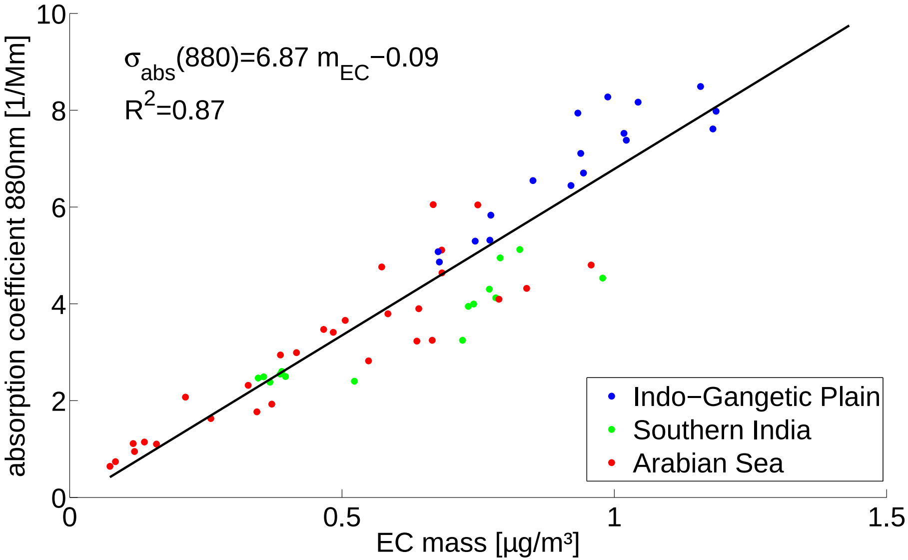

Figure 9. Particle absorption coefficient for 880 nm against $PM_{2.5}$ EC mass concentration, grouped by source regions according to Fig. 2.

ACPD
15, 3907–3953, 2015